Numerical Simulation of Friction Stir Spot Welding Process for Aluminum Alloys

Dongun Kim[1], Harsha Badarinarayan[2], Ill Ryu[3], Ji Hoon Kim[4], Chongmin Kim[5], Kazutaka Okamoto[6], R. H. Wagoner[7], and Kwansoo Chung[1,*]

[1] Department of Materials Science and Engineering, Research Institute of Advanced Materials, Seoul National University, San 56-1, Shillim-dong, Gwanak-gu, Seoul 151-742, Korea
[2] Research and Development Division, Hitachi America Ltd., 34500 Grand River Avenue, Farmington Hills, MI 48335, USA
[3] Department of Materials Science and Engineering, Stanford University, Stanford, CA 94305-2205, USA
[4] Materials Deformation Group, Korea Institute of Materials Science, 531 Changwondaero, Changwon-si, Gyeongnam 641-831, Korea
[5] Materials and Process Lab., R&D Center & NAO Planning, General Motors Corporation, Warren, MI 48090-9055, USA
[6] Hitachi Research Laboratory, Hitachi Ltd., Omika 7-1-1, Hitachi 319-1292, Japan
[7] Department of Materials Science and Engineering, The Ohio State University, 2041 College Road, Columbus, OH 43210, USA

Thermo-mechanical simulations of the Friction Stir Spot Welding (FSSW) processes were performed for AA5083-H18 and AA6022-T4, utilizing commercial Finite Element Method (FEM) and Finite Volume Method (FVM) codes, which are based on Lagrangian and Eulerian formulations, respectively. The Lagrangian explicit dynamic FEM code, PAM-CRASH, and the Eulerian Computational Fluid Dynamics (CFD) FVM code, STAR-CD, were utilized to understand the effect of pin geometry on weld strength and material flow under the unsteady state condition. Using FVM code, material flow patterns near the tool boundary were analyzed to explain weld strength difference between welds by a cylindrical pin and welds by a triangular pin, whereas the frictional energy concept using the FEM code had a limited capacity to explain the weld strength difference.

Keywords: metals, welding, strength, computer simulation, thermo-mechanical analysis

1. INTRODUCTION

Friction Stir Spot Welding (FSSW) is an evolving technique that has been rapidly gaining momentum since the beginning of this decade and has already found its place in commercial applications in the automotive industry, especially to replace conventional welding techniques including the Resistance Spot Welding (RSW), which showed poor weldability for advanced high-strength steels as well as aluminum alloys [1-6]. Although the principle of FSSW is similar to that of linear Friction Stir Welding (FSW), the process is much more complex in the sense that the actual welding time itself is short but the process dynamics involved are still

similar – tool plunge, material mixing (during dwell time) and tool retraction. FSSW can be considered as an unsteady state (transient) process whereas linear FSW is a steady state process, especially for the linear welding process [7,8].

After a rotating tool is plunged into workpieces in a lap configuration, the tool rotates for a few seconds without translation motion, which is the dwelling process. The rotating tool is then retracted from workpieces. Heat is generated by plastic dissipation at workpieces stirred by the rotating tool as well as by the friction between the tool and the workpieces. The workpieces stirred and softened by heat are ultimately joined together during the FSSW process. The advantages of FSSW include low residual stress and low energy input compared to the conventional welding method. One way to optimize the process is to utilize the thermo-mechanical modeling of FSSW.

The key parameters to judge the performance of FSSW are tool geometry, tool rotational speed, plunge depth and hold (dwell) time. Each of these parameters has an influence on the weld in terms of heat input, material mixing and weld cycle time, all of which are crucial to achieving a sound weld in terms of strength and morphology. The heat generated at the interface between the tool and the workpiece is an important aspect in making good welds. The temperature generated by the FSW process ranges from 80 % to 90 % of the melting temperature of the welding material, as measured by [9] and [10]. The amount of the heat input into the workpieces dictates the quality of the spot weld (in terms of static strength, micro-structure, residual stress etc.).

The scope of this paper is to develop a simulation model to predict weld performance after the FSSW process in terms of weld strength as well as morphology. The Computational Fluid Dynamics (CFD) Finite Volume Method (FVM) code STAR-CD [11] as well as the explicit dynamic FEM code PAM-CRASH [12] were used. The FSSW process consists of plunging, dwelling and retracting steps. Unlike linear FSW [7,8], FSSW cannot be considered as a steady state process wherein the whole welding process is conducted in a short time and consists only of a short dwelling step.

In the FVM model, the FSSW process was simulated as a coupled thermo-mechanical analysis, using the moving (rotating) mesh method. Two pin geometries, cylindrical and triangular, were considered to explain their effect on weld strength difference, as related with hook formation. In the FEM model, the FSSW process was simulated to evaluate the effect of various tool geometries on weld strength. Here, unlike in Eulerian simulations, frictional boundary conditions were imposed at the interface between the tool and the material. Contact energy and contact force were then used as criteria for spot weld strength, since the driving force for the spot formation is the energy produced by the contact between the tool and the sheets. Note that the FEM model was applied first just for the preliminary evaluation of the effect of various tool geometries on weld strength based on mechanical analysis only. The thermo-mechanical FVM simulation was then performed later for the detailed understanding of the cause of the strength difference considering the two pin geometries, which showed a major difference.

2. THEORY

For the thermo-mechanical analysis of FSW processes, the continuity equation as well as the momentum and energy conservation equations was solved with temperature dependent material properties. The mechanical property was assumed rate-insensitive and incompressible rigid-perfect Mises plastic [7,8] based on the normality rule; i.e.,

$$\mathbf{S} = 2\mu \mathbf{D}$$

$$\mathbf{D} = \dot{\bar{\varepsilon}}\frac{\partial \bar{\sigma}}{\partial \mathbf{S}} = \frac{3\dot{\bar{\varepsilon}}}{2\bar{\sigma}}\mathbf{S} = \frac{\mathbf{S}}{2\mu} \text{ and } \bar{\sigma} = \sqrt{\frac{3}{2}\mathbf{S}\cdot\mathbf{S}}, \ \dot{\bar{\varepsilon}} = \sqrt{\frac{2}{3}\mathbf{D}\cdot\mathbf{D}} \ (1)$$

where $\mathbf{D}$ and $\mathbf{S}$ are the rate of deformation and deviatoric Cauchy stress tensors, respectively, and $\bar{\sigma}$, $\bar{\varepsilon}$ and μ are the Mises effective yield stress, conjugate effective strain rate and viscosity, respectively. The yield stress $\bar{\sigma}(T)$ is temperature (T) dependent and the viscosity $\mu(T, \bar{\varepsilon})$ is dependent on temperature and strain rate as, from Eq. 1,

$$\mu = \frac{\bar{\sigma}}{3\dot{\bar{\varepsilon}}} \tag{2}$$

The momentum conservation equation is

$$\nabla \cdot \sigma + \rho \mathbf{b} = \rho \frac{D\mathbf{v}}{Dt}, \tag{3}$$

where σ is the Cauchy stress tensor, ρ is density, $\mathbf{b}$ is the acceleration of body force, $\mathbf{v}$ is a velocity vector and t is time, respectively, while D/Dt is the material time derivative and the density $\rho(T)$ is temperature dependent. The boundary condition of Eq. 3 is either the distribution of velocity or traction. The continuity equation is given as

$$\mathbf{v} \cdot \nabla \rho + \frac{\partial \rho}{\partial t} = 0, \tag{4}$$

where $\partial/\partial t$ is the spatial time derivative.

The energy conservation equation [13] is

$$\rho C_P \frac{DT}{Dt} = \nabla \cdot (k\nabla T) + \dot{Q}, \tag{5}$$

where C_p is the specific heat, k is the thermal conductivity and Q is the heat generation rate by plastic dissipation. The specific heat $C_p(T)$ and the thermal conductivity $k(T)$ are temperature dependent, while the heat generation rate Q becomes

$$\dot{Q} = \alpha \mathbf{S} : \mathbf{D}, \tag{6}$$

where α is the conversion factor (α was assumed to be 1.0 in this work).

The convective heat boundary condition of Eq. 5 is given by

$$\nabla T = \frac{h}{k}(T - T_B), \tag{7}$$

where h is the convective heat transfer coefficient and T_B is the surrounding temperature.

3. EXPERIMENTAL PROCEDURE

3.1. Welding process

FSW was performed on sheets of AA5083-H18 (upper sheet thickness of 1.64mm and lower sheet thickness of 1.24 mm) and AA6022-T4 (sheet thicknesses of 1.0 mm) by using a CNC controlled 3-D Linear FSW system called a
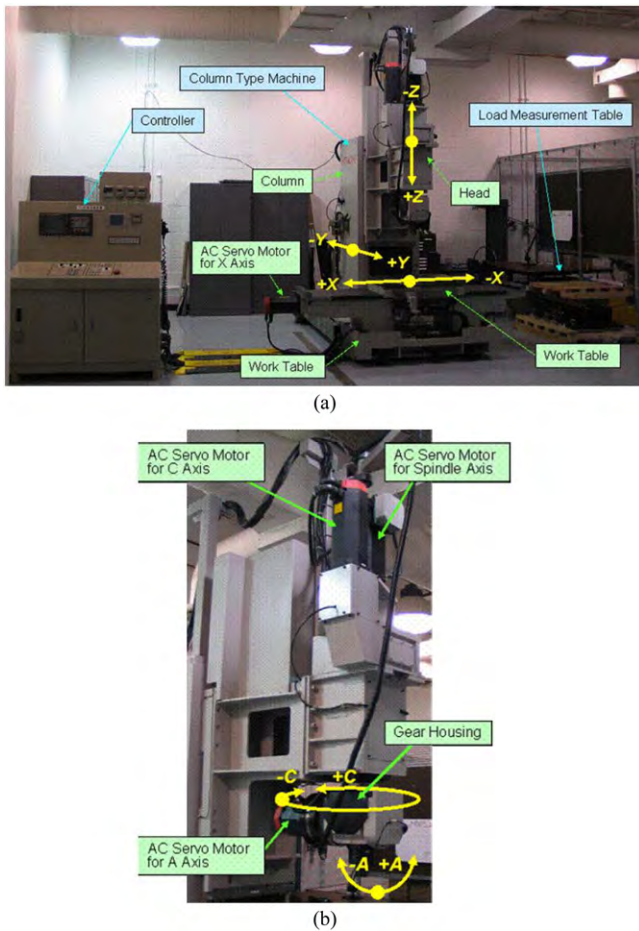
Fig. 1. CNC controlled 3-D linear FSW system 'HitSpin type GR3DC5T': (a) 3-D FSW system 'HitSpin' and (b) the machine head.

"HitSpin type GR3DC5T" that had a 7.5 KW spindle servo-motor (the spindle motor can operate up to 3000 rpm). As shown in Fig. 1, this system has 6 axes, i.e., X, Y, Z, A, C-axis and Spindle. The axial load capacity is designed up to 10 kN, which corresponds to about 5 mm weld depth for aluminum and magnesium alloys. The chemical compositions of the AA5083-H18 and the AA6022-T4 sheets are shown in Table 1 [14].

Table 1. The chemical composition for AA5083-H18 and AA6022-T4 in wt.%

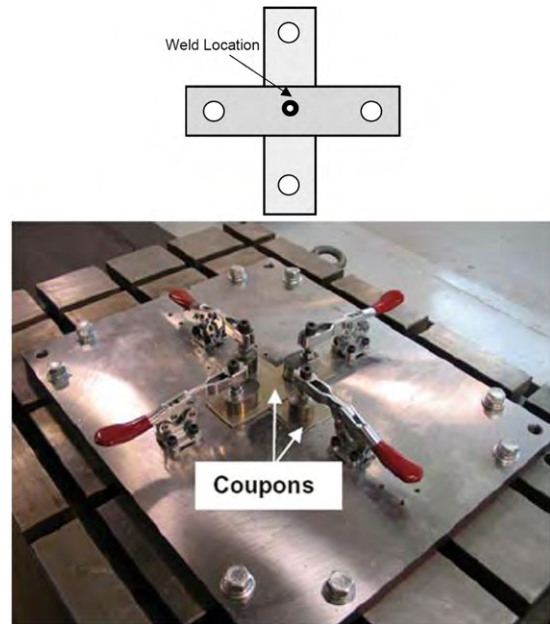| Component	AA5083-H18	AA6022-T4
Aluminum, Al	92.4 - 95.6 %	96.7 - 98.7 %
Chromium, Cr	0.0500 - 0.250 %	<= 0.100 %
Copper, Cu	<= 0.100 %	0.0100 - 0.110 %
Iron, Fe	<= 0.400 %	0.0500 - 0.200 %
Magnesium, Mg	4.00 - 4.90 %	0.450 - 0.700 %
Manganese, Mn	0.400 - 1.00 %	0.0200 - 0.100 %
Silicon, Si	<= 0.400 %	0.800 - 1.50 %
Titanium, Ti	<= 0.150 %	<= 0.150 %
Zinc, Zn	<= 0.250 %	<= 0.250 %

Fig. 2. Welding jig with a coupon in a cross-tension configuration.

Welds were made in a cross-tension configuration with coupon dimensions being 150 mm × 50 mm, as shown in Fig. 2 with the jig used for welding [15]. The specific reason for welding to be done in this cross-tension configuration was that welded coupons were to be implemented in an application in which the structure was subjected to uniaxial tension loading normal to the welds. Since the purpose of this study was to evaluate the effect of tool geometry on static strength, the weld parameters were fixed as follows: the tool rotation speed was 1,500 rpm for AA5083-H18 and 2,500 rpm for AA6022-T4, while the plunge and retract speeds were 20 mm/min and the dwell time was 2 s. These weld parameters gave reasonable results when used in a pre-liminary study [16]. The tool was made of tool steel H13 with several tool geometries, as shown in Fig. 3 with tool dimensions [17].
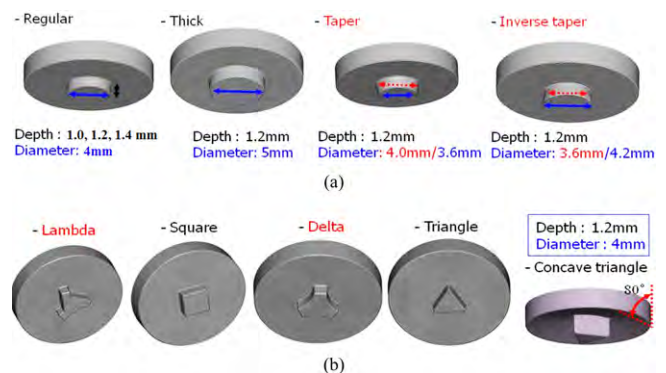

Fig. 3. Pin geometries, (a) conventional tool, (b) unconventional tool with 12 mm shoulder diameter.

3.2. Weld characterization

Cross sectional macro- and micro-structures of welds were examined by using an optical microscope for the AA5083-H18 sheet. Metallographic specimens were cold mounted in self-curing resin, and then subjected to mechanical grinding up to 2400 grit SiC paper and polishing with 0.05 μm silica suspension [18]. The specimens were also tested for weld strength on an Instron screw driven test machine at a constant crosshead speed of 5.0 mm/min.

4. THERMO-MECHANICAL MODELING

4.1. FEM under the Lagrangian description

4.1.1. Model description and boundary condition

The mechanical simulation of the FSSW process for AA6022-T4 was performed using the explicit dynamic FEM code PAM-CRASH [12] without thermal analysis. In this FEM analysis, the plunging and dwelling steps were simulated as an unsteady process. Large deformation and severe contact conditions were simulated with the mass scaling method and the damage elimination model option, in view of saving computational time and achieving better numerical convergence. If the time step of an element becomes smaller than the given mass scaling time step, the code adjusts its mass density such that its time step equals the given mass scaling time step. This option is useful in finite element meshes where element sizes are small but vary and can lead to important savings in computational time without noticeable deterioration of the solution. The damage elimination model assumes that, when the equivalent plastic strain reaches a specific value, at an integration point, the material point fails so that all the stress components are set to zero (with ultimate mesh elimination when all integration points fail). In order to understand the tool geometry effect on spot weld strength, tools of the various shapes shown in Fig. 3 were tried.

The process consists of a rotating tool that plunges into the workpiece in a lap configuration as shown in Fig. 4. In the experiments, the tool rotation speed was 2,500 rpm, while the plunge and retract speeds were 20 mm/min and the dwell time was 2.0 s. However, the whole process was assumed to be much faster in simulation to save computational time: the
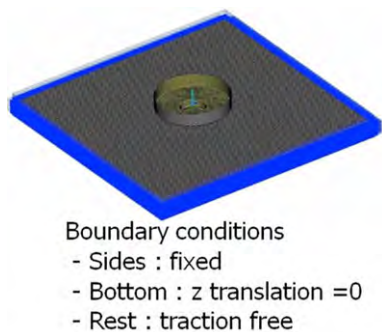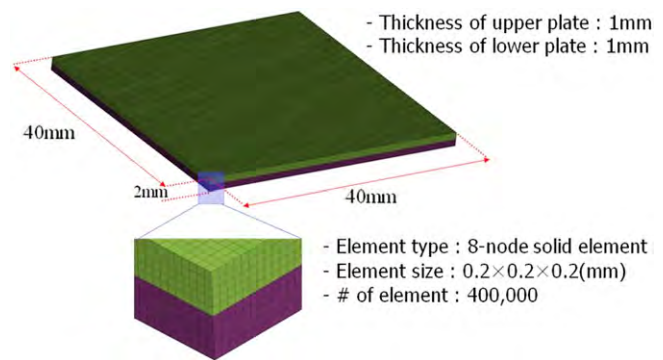

Fig. 5. Dimension of the meshes.

tool was plunged for 5.0 ms at the speed of 600 mm/s, and dwells for 5.0 ms with the rotating speed of 12,000 rpm. The simulation was intended only for the qualitative understanding of the tool geometry effect.

The model description and dimensions are shown in Fig. 5, in which the workpiece dimension is 40 mm × 40 mm × 1 mm (the sheet thickness for AA6022-T4). For two sheets in a lap configuration, two separate workpieces were employed for simulation and a total of 400,000 solid elements were implemented with the element size of 0.2 mm × 0.2 mm × 0.2 mm while the tool was modeled as a rigid body. As for the boundary conditions, the sides of two sheets were fixed and the bottom surface of the lower sheet was constrained not to move up and down, while the rest was free traction including the contact surfaces between the two sheets, as shown as in Fig. 4.

The contact (friction) force and energy were calculated to predict the effect of tool geometry on spot strength, since the driving force of the formation of the spot weld was the friction energy resulting from the contact. The friction coefficient was 0.2 and the friction energy was the integration of the tangential frictional force multiplied by the relative velocity of the two contacting surfaces.

4.1.2. Material Property

For simplicity in the FEM simulation of the FSSW process, the property of the AA6022-T4 was assumed to be elasto-linear hardening Mises plastic without rate and temperature dependence, as shown in Table 2 [19-21].

Fig. 4. Schematic model description and boundary conditions.

Table 2. Material properties of AA6022-T4 at room temperature

Material property	AA6022-T4
Density(Kg/m^3)	2,690.0
Young's Modulus(GPa)	69.0
Yield Stress(MPa)	172.0
Poisson Ratio	0.33
Hardening Modulus(GPa)	1.0
Maximum plastic strain for element elimination(damage model)	(1.5)

The value in the parenthesis is assumed one

4.2. FVM under the Eulerian Description

4.2.1. Model description

The thermo-mechanical simulation of the FSSW process for AA5083-H18 was performed using the CFD code STAR-CD [11]. The continuity equation as well as the momentum and energy conservation equations for the process was solved. The FSSW process consists of tool plunging, a short dwelling time and tool retracting steps. But, only the 2 s dwelling step in which the rotating tool was plunged into the workpiece in a lap configuration was simulated, as shown in Fig. 6. Two types of pins were considered: cylindrical and triangular pins with concave shoulders. Unlike Linear FSW, FSSW was considered as an unsteady state process wherein the whole welding process is conducted in a short time and consists of a short dwelling step.

The cylindrical and triangular pins both have 10 degree concave shoulders. The pin radius was 2.5 mm and the shoulder radius was 6 mm, while the pin length was 1.6 mm from the shoulder edge and the plunge depth of the shoulder was 0.2 mm. The diameter of the circle inscribed by the triangular pin was the same as the diameter of the cylindrical pin. The model description and dimensions are shown in Figs. 7 and 8 with 2.88 mm thickness (two workpieces in a lap configuration were considered as one piece) with the workpiece radius of 50 mm. Note that the central region with the radius of 8 mm was solved for plastic deformation, while
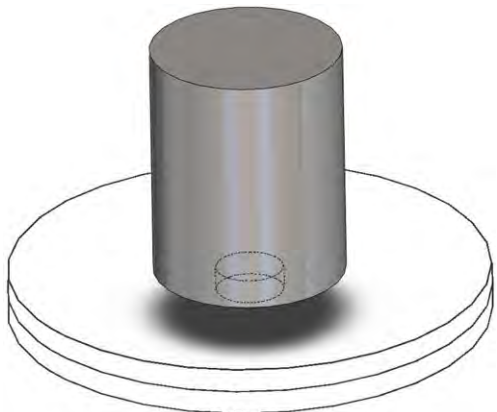

Fig. 8. The model dimension, (a) cylindrical pin and (b) triangular pin.

the rest was assumed to be a rigid body (but still subjected to the heat transfer problem) to reduce computational time. In total, 155,040 elements and 161,952 elements were used for the circular and triangular pin models, respectively.

4.2.2. Material properties

The rate-insensitive and incompressible rigid-perfect Mises plastic property was applied for the workpiece. Temperature

Table 3. Temperature dependent yield stress (OSU experiment) (Partially measured at OSU with $\dot{\varepsilon} = 10^{-2.5}$ and assumed values are within parentheses)

Temp. ($^{\circ}$C)	Y.S.(MPa)
20	440
100	437
200	364
300	181
400	61
(440)	(50)
(540)	(40)
(570)	(0)

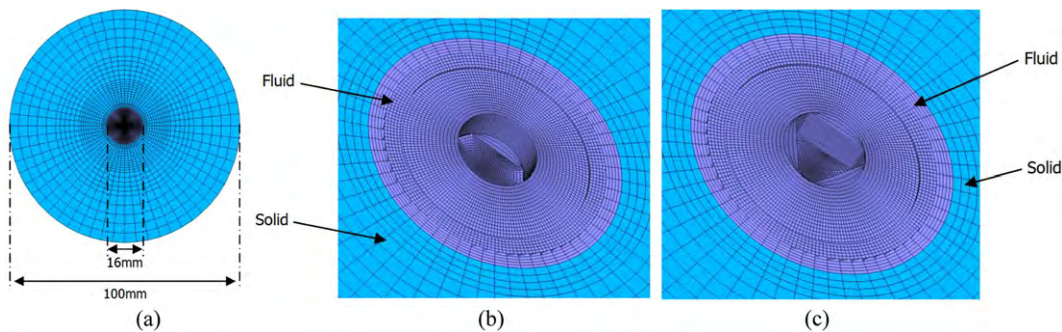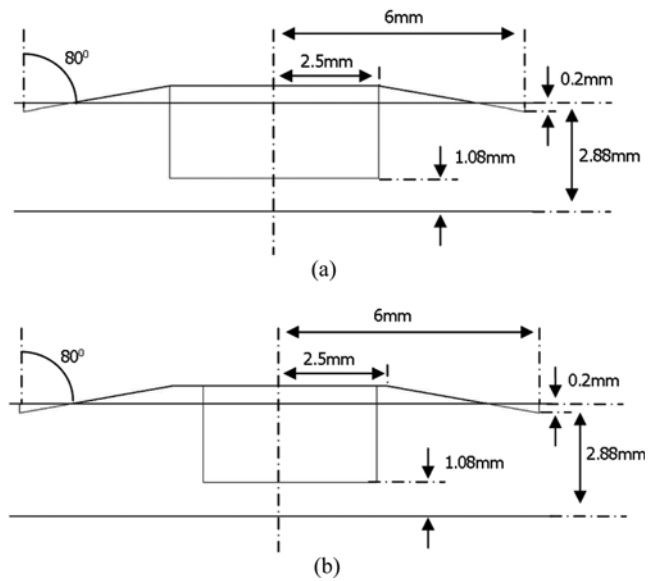

Fig. 6. Schematic views of the friction stir spot welding process.

Fig. 7. The model description, (a) top view, (b) cylindrical pin (155,040 cells) and (c) triangular pin (161,952 cells).

Table 4. Temperature dependent density, thermal conductivity and specific heat (calculated for AA5083-H18 from AA5052-H32 properties)

Temp. (°C)	Conductivity (W/m°C)	Specific heat (J/Kg°C)	Density (Kg/m³)
-20.0	112.5 (106.9)	924.1	2673.9
80.0	122.7 (120.7)	984.2	2642.7
180.0	131.6 (134.5)	1039.6	2629.4
280.0	142.3 (142.9)	1081.2	2611.5
380.0	152.5 (148.9)	1136.6	2589.3
480.0	159.5	1178.2	2567.0
580.0	177.2	1261.4	2549.2

Experiment values are in parenthesis
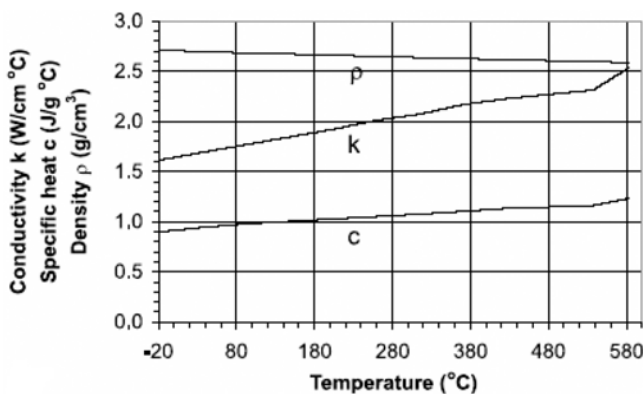
Fig. 9. Temperature dependent material properties for AA5052-H32.

dependent yield stresses for the AA5083-H18 sheets were used in this work as shown in Table 3, and these stresses were partially measured at OSU (with $\dot{\varepsilon} = 10^{-2.5}$). Since experimental yield stresses were available only up to 400 °C, decreasing yield stresses were assumed above 400 °C, considering that yield stresses vanish near the melting temperature of AA5083-H18 (574 °C [22]).

As for density and thermal properties, only the room temperature data was available for AA5083-H18 and its temperature dependent properties were not available, except partially for the thermal conductivity. Therefore, assumed temperature dependent properties were obtained from those of AA5052-H32 [23] by proportionally modifying the values considering the ratios of the values of the two materials at room temperature, as shown in Table 4. Note that Fig. 9 shows the temperature dependent thermal properties of AA5052-H32 and Table 5 shows the room temperature properties of AA5052-H32 and AA5083-H18 [19]. Considering the difference of the room temperature values, the assumed temperature dependent thermal properties of AA5083-H18

Table 5. Material properties of AA5083-H18 and AA5052-H32 at room temperature

Material property	AA5083-H18	AA5052-H32
Density(Kg/m³)	2,660.0	2,708.96
Thermal conductivity(W/m°C)	117.208	167.25
Specific heat(J/Kg°C)	962.412	932.57

were obtained from Fig. 9 as shown in Table 4. Note that the thermal conductivity measured for AA5083-H18 is very similar to the assumed properties, partially justifying the validity of the assumed values. The data in Table 4 was implemented in the user subroutine.

4.2.3. Boundary conditions

Since the FSSW process was simulated using the moving (rotating) mesh method, the central meshes with the radius of 8 mm were rotating with the tool rotation speed (at 1,500 rpm) to account for the rotating tool (without translation) of the dwelling process for 2 s. At all other boundaries except at
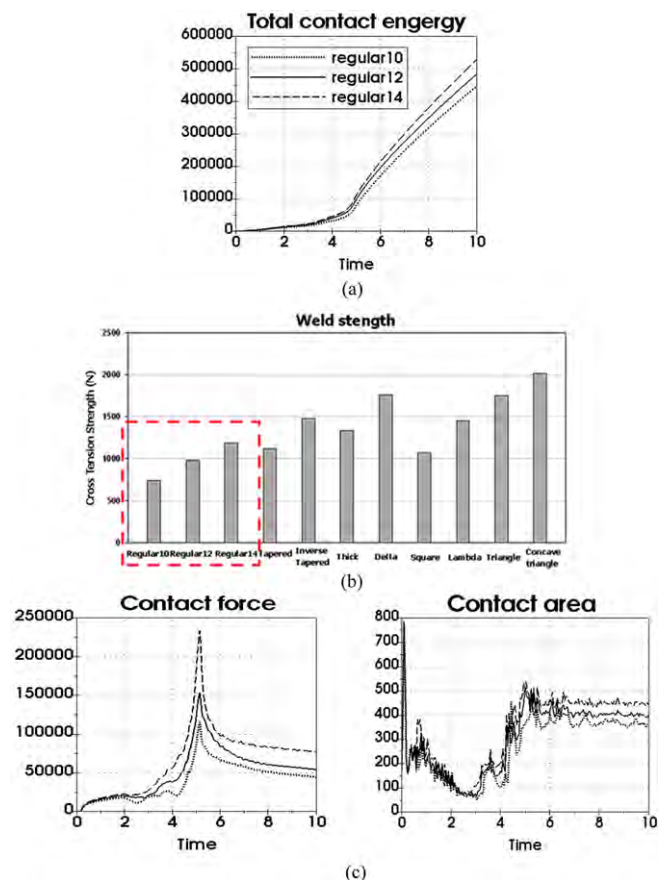
Fig. 10. Results for different pin depths of the conventional tools: (a) total contact energy (frictional energy), (b) measured weld strength and (c) contact force and area.

the boundary in contact with the tool, the free traction boundary condition was applied. At the tool boundary, the material was assumed to be in perfect contact with the tool and to rotate at the rotating speed of the tool; hence heat generation by interfacial friction was ignored.

The convective heat transfer coefficient of 30 W/m^2 $°$C was used for the top and sides of the work–piece which is typical for natural convection between aluminum and air [24]. At the bottom of the workpiece, the convective heat transfer coefficient was assumed to be 2,000 W/m^2 $°$C just below the tool, at the 8 mm radius region, considering that heat transfer between two contacting surfaces increases when the pressure between them increases under the tool [25]. For the remaining bottom surface, the coefficient was assumed to be 200 W/m^2 $°$C.

5. RESULTS

5.1. FEM under the Lagrangian description

In order to verify the numerical simulation results of these preliminary trials using the Lagrangian code, simulated frictional energy (or total contact energy) was compared with experimental spot weld strength, particularly as associated
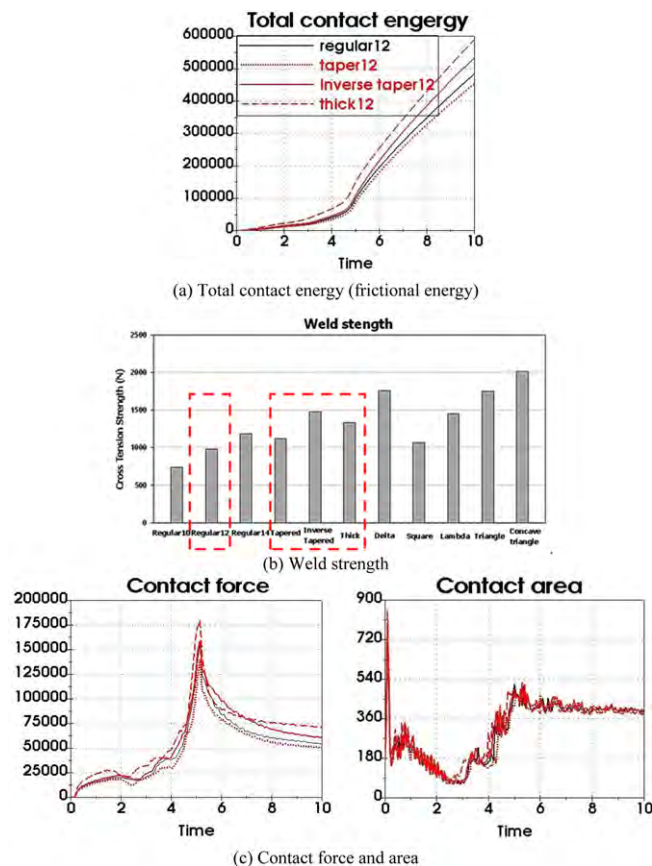
Fig. 11. Results for different taper pin shapes and thickness: (a) total contact energy (frictional energy), (b) measured weld strength and (c) contact force and area.
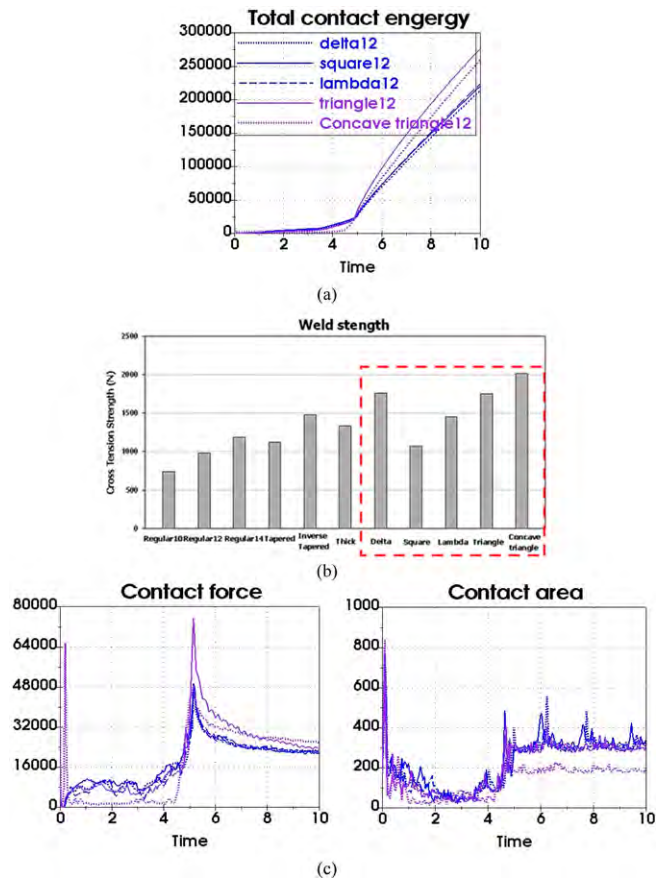
Fig. 12. Results for the unconventional tools: (a) total contact energy (frictional energy), (b) measured weld strength and (c) contact force and area.

with tool geometry. In the first category of tool geometry, the effect of pin depth (or length) in the conventional tools on spot strength was examined as shown in Fig. 10. As the pin depth increased, both the frictional energy and experimental weld strength increased, confirming the correlation between them. In the second category, the effect of taper pin shapes was examined, as shown in Fig. 11, for the inverse tapered pin, taper pin and thick pin (see Fig. 3 for their shapes). In the third category, the effect of the unconventional tools was examined as shown in Fig. 12. Unlike the first category, the second and third categories did not show good correlation between the fractional energy and measured weld strength. In particular, the frictional energy of the concave triangular pin was lower than that of the regular pin, while the measured weld strength of the concave triangular pin was almost twice as that of the regular pin. The cause of the weld strength discrepancy between the two tool shapes will be discussed in Section 5.2, based on the Eulerian simulation results.

5.2. FVM under the Eulerian description

Temperature profiles at the top surface for the cylindrical and triangular pins are shown at various moments in Fig. 13,
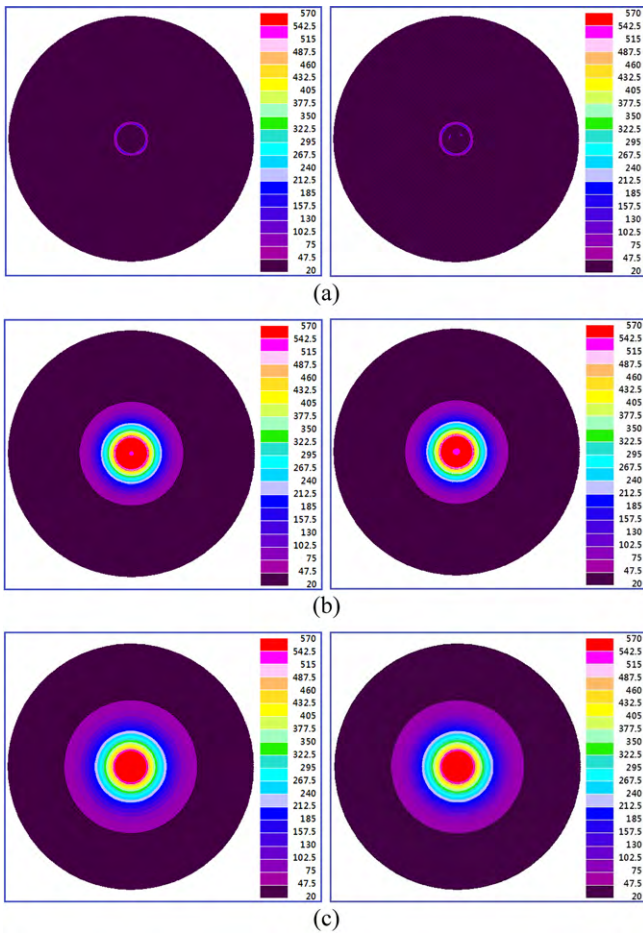
Fig. 13. Temperature history at the top surface as time procedure for the cylindrical pin and the triangular pin, (a) 94.05 °C (left-cylindrical) and 92.65 °C (right-triangular) after 0.01 s, (b) 561.45 °C (left-cylindrical) and 562.65 °C (right-triangular) after 1 s, and (c) 563.75 °C (left-cylindrical) and 564.55 °C (right-triangular) after 2 s.
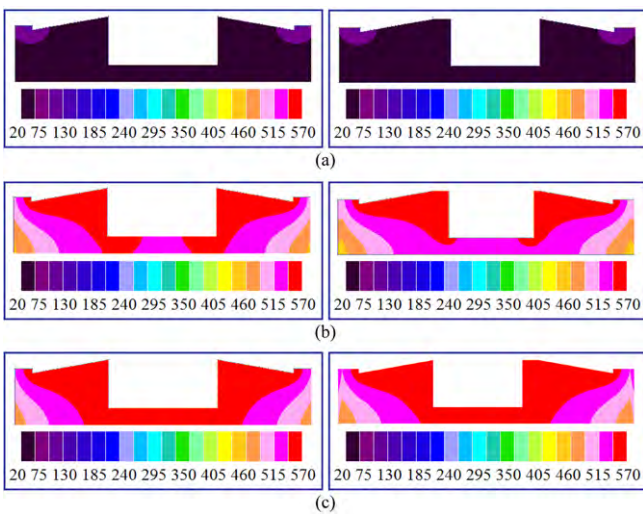

Fig. 14. Temperature history at the cross section near the tool as time procedure for the cylindrical pin and the triangular pin, (a) 94.05 °C (left-cylindrical) and 92.65 °C (right-triangular) after 0.01 s, (b) 561.45 °C (left-cylindrical) and 562.65 °C (right-triangular) after 1 s and (c) 563.75 °C (left-cylindrical) and 564.55 °C (right-triangular) after 2 s.

while Fig. 14 show temperature profiles at the cross section containing the middle of the tool. The temperature at the edge of the tool shoulder reached just below the melting temperature (574 °C [22]) in 0.3 s, after which the heat propagation was initiated. The peak temperature for the cylindrical pin was similar to that of the triangular pin since heat was mostly generated at the shoulder.

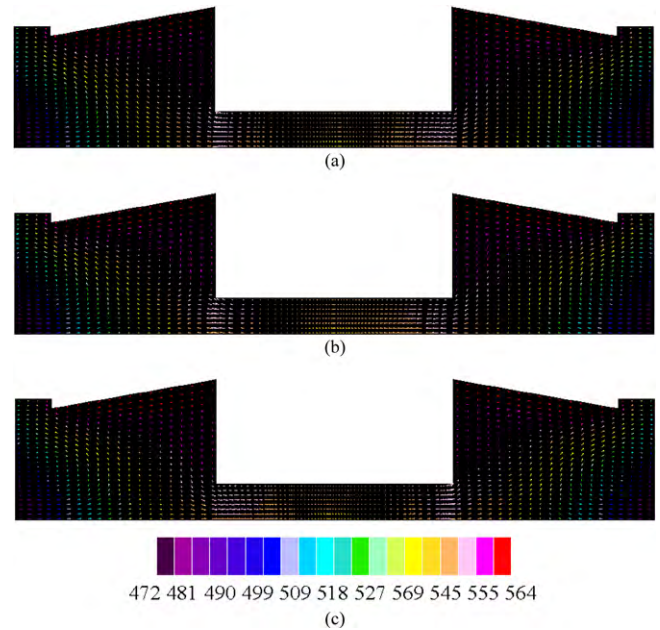Figures 15 and 16 show the material flow at the cross sec-

Fig. 15. Material flow direction at the cross section near the tool as time procedure for cylindrical pin, after (a) 1.94 s, (b) 1.95 s and (c) 1.96 s (in °C).
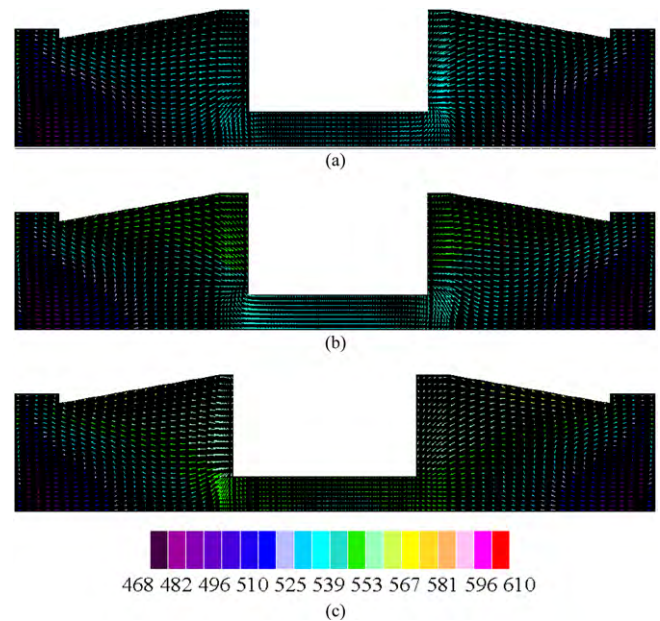

Fig. 16. Material flow direction at the cross section near the tool as time procedure for triangular pin, after (a) 1.94 s, (b) 1.95 s and (c) 1.96 s (in °C).

Fig. 17. The picture of the specimen after the tool suddenly stopped while welding for the concave triangular pin.

tion containing the middle of the tool for the cylindrical and triangular pins at various instances. For the cylindrical pin, materials near the tool did not move that much along the radial direction. However, for the triangular pin, materials near the pin boundary showed significant in and out motion along the radial direction, since the boundary of the triangular pin moved in and out along the radial direction during the tool rotation. Note that this simulation result, with the material moving in and out, was compatible with the experiment as shown in Fig. 17, which is the picture of the specimen after the tool suddenly stopped while welding for the triangular pin. Non-cylindrical pin geometry, like the triangular pin geometry, caused a severe change of the material flow pattern near the pin boundary [18].

Note that heat generation of the cylindrical and triangular pins was similar; only the material flow pattern was differ-
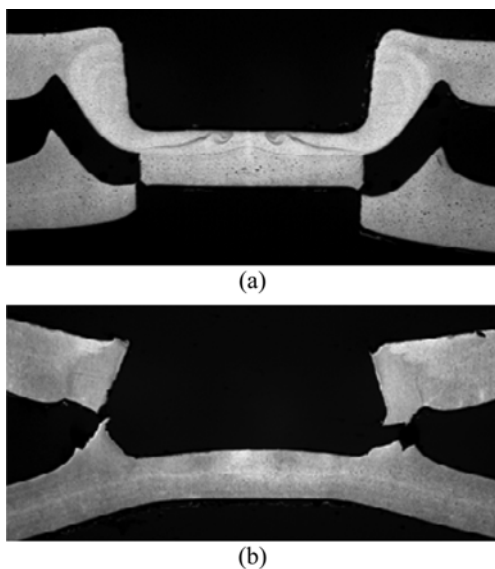

Fig. 18. Cross sectional macrographs showing crack propagation in the cross-tension test for (a) cylindrical pin (weld strength: 1,800N) and (b) triangular pin (weld strength: 3,600N) [18].

ent, which then caused the static weld strength to be different. The weld strength for the concave triangular pin was almost twice that of the concave cylindrical pin, as shown in Fig. 18 [18]. The triangular pin geometry yielded higher weld strength compared to the cylindrical pin, since the material flow pattern affected the hook formation near the pin boundary. The hook formation and top sheet thinning were key geometric characteristics of the friction stir welded specimen, significantly affecting the weld strength, as shown in Fig. 19 [18].

For welds made with the cylindrical pin, the hook runs gradually upward and then bypasses the stir zone and points downward towards the weld bottom, as shown in Fig. 20 [18]. For welds made with the triangular pin, the hook is
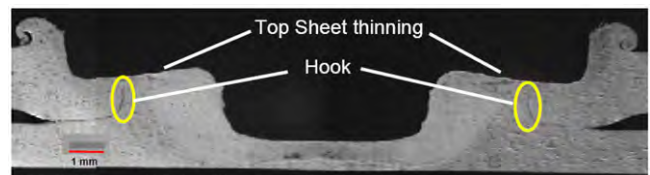

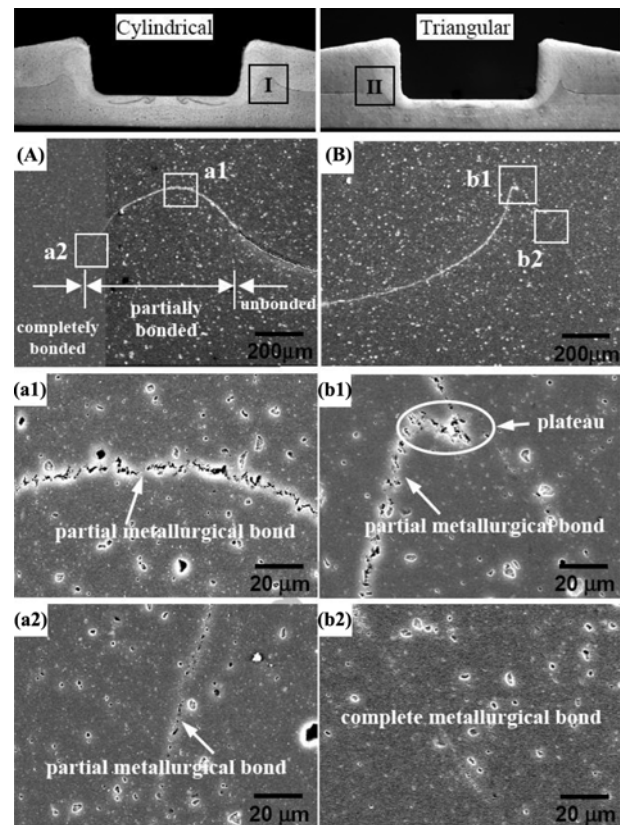**Fig. 19.** Micro-cross section at the weld center [17].

Fig. 20. Cross-sectional macrostructures of the welds for the cylindrical pin (left) and the triangular pin (right): (A) magnified view of the hook geometry in region I for welds by the cylindrical pin with (a1) and (a2) showing partial metallurgical bonding within region I at the locations indicated; (B) magnified view of the hook geometry in region II for welds by the triangular pin with (b1) and (b2) showing partial and complete metallurgical bonding in region II at the respective locations indicated [18].

directed upward towards the stir zone and ends with a very short plateau, as shown in Fig. 20. As reported by Fujimoto *et al.* [26], immediately next to the pin the material driven by pin threads moves downward from the upper sheet to the lower sheet, forming the major portion of the stir zone; the material originally from the lower sheet is pushed outward as well as upward towards the upper sheet. Therefore, the hook bulges upward in the region away from the keyhole and runs downward towards the bottom of the weld near the keyhole. In contrast, due to the asymmetric geometry of the triangular shaped pin, successive rotation of the pin is believed to enhance the plastic flow of the material in the vicinity of the pin in the radial direction, compared to the cylindrical, pin, causing the material to move back and forth in the radial direction, which results in the breaking-up (dispersion) of the hook in the stir zone .With the sustained hook, the weld with the cylindrical pin shows easy crack propagation along the hook lie in Fig. 18(a), resulting in the lower weld strength. The weld with the triangular pin does not show easy crack propagation in Fig. 18(b) because the hook was broken by the material mixture promoted by the radial back and forth motion as shown in Fig. 20(B).

6. SUMMARY

Thermo-mechanical modeling of the FSSW process was conducted using commercial FEM and FVM codes based on Lagrangian and Eulerian formulations, respectively. The Lagrangian FEM and Eulerian FVM codes were applied under the unsteady state condition to understand the effect of tool geometry on material flow and weld strength. The weld strength results for various tool geometries were predicted based on the frictional energy obtained from the Lagrangian FEM model, but this approach was acceptable only for relative comparison among regular (cylindrical) pin geometries. Using the concept of the material flow pattern, however, the Eulerian FVM simulation gave reasonable insight that different hook shapes near the pin formed by the triangular and cylindrical pins differentiated their weld strength.

ACKNOWLEDGMENTS

REFERENCE

1. R. Sakano, *et al.*, *Proceeding of the 3rd International Symposium on Friction Stir Welding*, TWI, Kobe, Japan (2001).
2. S. S. Park, S. M. Lee, Y. Cho, N. H. Kang, J. H. Yu, Y. S. Kim, and Y. D. Park, *J. Kor. Inst. Met. & Mater.* **46**, 672 (2008).
3. J. W. Son, Y. D. Park, M. J. Kang, and D. C. Kim, *J. Kor. Inst. Met. & Mater.* **47**, 834 (2009).
4. S. M. Lee and Y. D. Park, *J. Kor. Inst. Met. & Mater.* **48**, 71 (2010).
5. P. H. Thornton, A. R. Krause, and R. G. Davies, *Weld. J.* **75**, 101s (1996).
6. A. Gean, S. A. Westgate, J. C. Kucza, and J. C. Ehrstrom, *Weld. J.* **78**, 80s (1999).
7. D. Kim, H. Badarinarayan, J. H. Kim, C. Kim, K. Okamoto, R. H. Wagoner, and K. Chung, *Eur. J. Mech. A-Solids* **29**, 204 (2010).
8. J. H. Kim, F. Barlat, C. Kim, and K. Chung, *Met. Mater. Int.* **15**, 125 (2009).
9. W. Tang, X. Guo, J. C. McClure, L. E. Murr, and A. Nunes, *J. Mater. Process. Manu.* **7**, 163 (1988).
10. P. A. Colegrove, M. Painter, D. Graham, and T. Miller, *Proceedings of the 2nd International Symposium on Friction Stir Welding*, TWI, Gothenburg, Sweden (2000).
11. CD-Adapco, STAR-CD 3.26 (2005).
12. ESI, PAM CRASH (2006).
13. A. J. M. Spencer, *Continuum Mechanics*, p. 100-101, Dover Publication Inc., Mineola, New York (2004).
14. Metals Handbook, Vol. 2, Properties and Selection: Non-ferrous Alloys and Special-Purpose Materials, ASM International 10th Ed., p.19 (1990).
15. H. Badarinarayan, Q. Yang, and F. Hunt, *Paper #2008-01-0147*, SAE World Congress & Exhibition, SAE, Detroit, MI, USA (2008).
16. F. Hunt, K. Okamoto, and H. Badarinarayan, *Paper #2006-01-0970*, SAE World Congress & Exhibition, Detroit, MI, USA (2006).
17. H. Badarinarayan, Q. Yang, F. Hunt, and K. Okamoto, *Proceedings of the 7th International Symposium on Friction Stir Welding*, TWI, Awaji Island, Japan (2008).
18. H. Badarinarayan, Q. Yang, and S. Zhu, *Int. J. Mach. Tool. Manu.* **49**, 142 (2009).
19. Metals Handbook, Vol.1, Properties and Selection of Metals, 8th ed., p. 944, ASM (1961).
20. J. F. Wang, R. H. Wagoner, W. D. Carden, D. K. Matlock, and F. Barlat, *Int. J. Plasticity* **20**, 2209 (2004).
21. P. M. Dixit and U. S. Dixit, *Modeling of Metal Forming and Machining Processes*, 1st ed., p. 414, Springer (2008).
22. Metals Handbook, Vol. 2, ASM International 9th ed., p.104 (1979).
23. X. K. Zhu and Y. J. Chao, *Comput. Struct.* **80**, 967 (2002).
24. Y. J. Chao, X. Qi, and W. Tang, *Transactions of the ASME* **125**, 138 (2003).
25. T. Hyoe, P. A. Colegrove, and H. R. Shercliff, *Proceeding of TMS Spring Meeting, Friction Stir Welding II*, TMS, San Diego, CA, USA (2003).
26. M. Fujimoto, S. Koga, N. Abe, Y. S. Sato, and H. Kokawa, *Q. J. Jpn. Weld. Soc.* **26**, 67 (2008).